Comprehensive model for the electronic transport in Pt/$SrTiO_3$ analog memristive devices

Carsten Funck,[1] Christoph Bäumer,[1,4] Stefan Wiefels,[1] Tyler Hennen,[1] Rainer Waser,[1,2,3] Susanne Hoffmann-Eifert,[3] Regina Dittmann,[2] and Stephan Menzel[2]

[1]*Institute for Electronic Materials II and JARA-FIT, RWTH Aachen University, Sommerfeldstrasse 24, Aachen 52074, Germany*
[2]*Peter Grünberg Institute 7 and JARA-FIT, Research Center Jülich Wilhelm-Johnen-Strasse, 52428 Jülich, Germany*
[3]*Peter Grünberg Institute 10 and JARA-FIT, Research Center Jülich Wilhelm-Johnen-Strasse, 52428 Jülich, Germany*
[4]*Department of Materials Science and Engineering, Stanford University, Stanford, California 94305, USA*

(Received 23 March 2020; revised 22 June 2020; accepted 25 June 2020; published 21 July 2020)

The presented study considers the electronic conduction across a $SrTiO_3$/Pt Schottky electrode in a resistive switching cell. It is generally accepted that the resistive switching effect is based on the migration of oxygen vacancies, which can be understood as mobile donors. In the experimental approach, a Nb:$SrTiO_3$/$SrTiO_3$/Pt resistive switching cell is fabricated and tested for its electronic and resistive switching characteristics. Using different voltage stimuli, several analog resistance states are realized. Afterwards, the electrical transport properties under different applied voltages and temperatures are measured for each analog resistive state. To gain physical insight into the analog resistive switching a numerical simulation model is developed. The electronic conduction is calculated based on the single band transport theory and a phonon scattering theory accounting for polar material systems. The simulation model allows testing of the conduction in these resistive switching cells by using different doping (oxygen vacancy) concentrations. Combining the simulation model and the experiment, it delivers a comprehensive physical description for the conduction. By means of simulation, the energy resolved current transport across the Schottky barrier is analyzed. It forms a peaklike distribution, originating from the limited thermal excitation and tunneling probability across the $SrTiO_3$/Pt Schottky barrier. Thus, the conduction processes in all states are identified as a balance between a thermally assisted tunneling effect and a phonon dominated bulk transport. Applying this understanding, the resistive switching effect is reduced to a modification of the Schottky tunnel barrier, based on the rearrangement of oxygen vacancies. Thus a low vacancy concentration leads to a high and wide tunneling barrier, which is reduced and shortened for higher concentrations. All resistance states in between are understood as an adjustment of intermediate tunneling barriers. The physical insights leading to the realization of analog resistance states is mandatory to realize new types of neuromorphic computing circuits based on resistive switching devices. Furthermore, the obtained results could be easily transferred to other systems where a static doping concentration applies. This makes the results highly interesting to other applications in the field of electronic oxides and Schottky barrier dominated systems.

DOI: 10.1103/PhysRevB.102.035307

I. INTRODUCTION

In the field of nonvolatile memory devices and neuromorphic computing, redox-based resistive switching memories (abbreviated as ReRAMs) are intensively studied, because of their promising properties for nonvolatile data storage such as high endurance, long retention, fast switching kinetics, and low switching energy [1–18]. One type of redox-based resistive switching device is the valance change mechanism (VCM). Here, an insulating (transition) metal oxide is sandwiched between two metal electrodes [19], and the bipolar resistive switching phenomenon is invoked by an initial electroforming step [20]. The electroforming process generates an electrical conducting filamentary region consisting of a high concentration of oxygen vacancies. During the forming step, the oxide material is locally reduced by extracting oxygen probably via an interface reaction [21]. The enhanced conduction stems from the properties of oxygen vacancies, which form a shallow donor-type defect state in many materials [22]. The typical resistive switching behavior of these VCM cells is based on a concentration change of oxygen vacancies at the current dominating metal electrode. In the case of a SET process the oxygen vacancy concentration is increased, which switches the device into the low resistive states (LRSs). The reverse process of lowering the vacancy concentration is named RESET and turns the cell to the high resistive states (HRSs). Thus, the SET and RESET are the names of the operations which switch the VCM cell into the LRSs and HRSs, respectively. To initiate the SET and the RESET, external voltage stimuli V_{SET} and V_{RESET} with opposite polarity are required, respectively. The change of the concentration at the interface can be realized by different mechanisms, for instance, due to a reconfiguration of oxygen vacancies in the filament or by an exchange of oxygen vacancies with metal electrode [23–25]. The mechanism determines the polarity of V_{SET} and V_{RESET} [23,25]. Independent of the underlying mechanism, the electrode where the oxygen vacancy concentration is modified is called the active electrode. Typically, nonidentical metal electrodes are applied to VCM cells and the active electrode is obtained by the high work function (Schottky barrier) electrode. A detailed introduction to the VCM cells can be found in recent review articles and textbooks [26–29].

Depending on the resistive switching cell, several intermediate states can be programmed, leading to an analog switching, which can be used to increase the information storage density [30–34]. Furthermore, analog resistive switching is of immense interest to enable computing networks which create a virtual synapsis using resistive switches [31,35–38]. Thus, a physical understanding of the analog nature of these devices and their electronic conduction properties has the potential to pave the way towards new computing concepts.

Previous studies identified the conduction mechanism for the LRS using density functional theory [39,40]. However, those studies only focus on the LRS conduction, and do not allow conclusions about the HRSs or different analog resistance states. The combination of dedicated experiments with an extended simulation model is mandatory to provide a complete physical understanding of the technological important feature of analog switching.

These issues will be addressed in the present study by using the model system Nb:$SrTiO_3$/$SrTiO_3$/Pt, where the active electrode is formed by the Schottky contact at the Pt metal electrode. To this end, the voltage dependence of the electronic current is measured for different analog resistance states at various temperatures. This enables us to identify trends in the current voltage dependence and to derive a physical description of the current transport mechanism through a numerical modeling based on Fermi-Dirac statistics and single band transport theory. The simulation model includes current transport contributions via thermionic emission, thermally assisted tunneling, and direct tunneling. In addition to the interface contribution, the bulk transport is considered by the theory of scattering in polar systems. Taking all possible contributions into account, the simulation model is able to reproduce the unique transport properties observed in the electrical measurements under different thermal conditions for all programmable resistance states. The results of this study are neither restricted to one Schottky system nor to resistive switching systems in general. The conclusions apply to other systems with static constant doping, especially for high band-gap semiconductor materials.

II. EXPERIMENT

For the experimental investigations, a 10-nm crystalline $SrTiO_3$ switching layer is deposited on 0.5-wt % Nb:$SrTiO_3$ by pulsed laser deposition as described in Ref. [41]. The $SrTiO_3$ thin film is covered by a Pt electrode and structured to a cell size of 13×19 μm^2 [39,41]. This leads to the model VCM system Nb:$SrTiO_3$/$SrTiO_3$/Pt. The active (Schottky-type) electrode is formed by the $SrTiO_3$/Pt interface. For all electrical measurements, the signal is applied to the active Pt electrode. To invoke resistive switching behavior, an initial forming step is applied [cf. the red curve in Fig. 1(a)], with a current compliance of 50 mA under ambient conditions and a temperature of 300 K. Afterwards, the typical resistive switching behavior is obtained, shown as the black curve in Fig. 1, under the same conditions. The forward direction of the Schottky electrode corresponds to the SET polarity at positive voltages and the reverse direction to the RESET polarity at negative voltages [1,25].

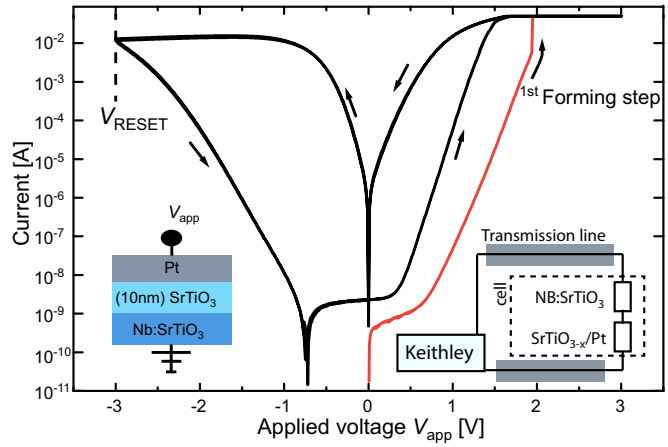

FIG. 1. Measurement of a typical resistive switching curve (black). Red shows the electroforming cycle.

For the LRSs, density functional theory simulation suggested a transition from a thermally activated tunneling process at low voltages to a direct tunneling/bulk limited transport at higher voltages, in the case of a reverse biased Schottky contact [39]. This transition can be identified due to the opposite temperature dependences of current flows in the two voltage regimes. This effect induces a crossing in the *I-V* measurements for different temperatures [Fig. 2(a)] [39]. So far, this effect has neither been reported in the LRS Schottky forward direction nor in the HRSs.

Here, the LRS is investigated for a wide voltage range in the Schottky forward direction. The SET process, switching the device to the LRS, is interrupted at a current compliance of 50 mA. Thus, the tested voltage range is chosen to keep the current below 50 mA, to avoid additional changes in ionic configuration. This allows an approximation of the LRS as a constant resistance state, with defined electronic transport properties. The *I-V* measurements for the forward (SET) polarity are shown in Fig. 2(b) in comparison to the reverse direction [cf. Fig. 2(a)]. Indeed an intersection effect could be observed in the current-voltage-temperature (*I-V-T*) measurements, but at higher absolute voltages compared to the reverse Schottky direction. While the similarities suggest the same transport mechanisms for the forward and reverse directions, it remains unclear which mechanism induces the intersection shift towards higher absolute voltages. Thus, a more detailed discussion is required for a comprehensive understanding.

In contrast to the SET, the RESET is a self-limiting process. Marchewka *et al.* suggested that this self-limiting process is a result of two competing forces [42]. Thus, intermediate states can be programmed by choosing the reset stop voltage V_{RESET}. For the resistive switching *I-V* loop shown in Fig. 1 the RESET stop voltage V_{RESET} is marked.

In the following, the analog resistive switching nature is tested by interrupting the RESET at different amplitudes V_{RESET}. Due to the importance of the ambient conditions the SET and RESET are only applied at ambient atmospheric conditions with a temperature of 296 K [43]. Initially, we initiate one single SET process in advance (cf. Fig. 1). Afterwards several RESET sweeps are applied in a row, thereby the

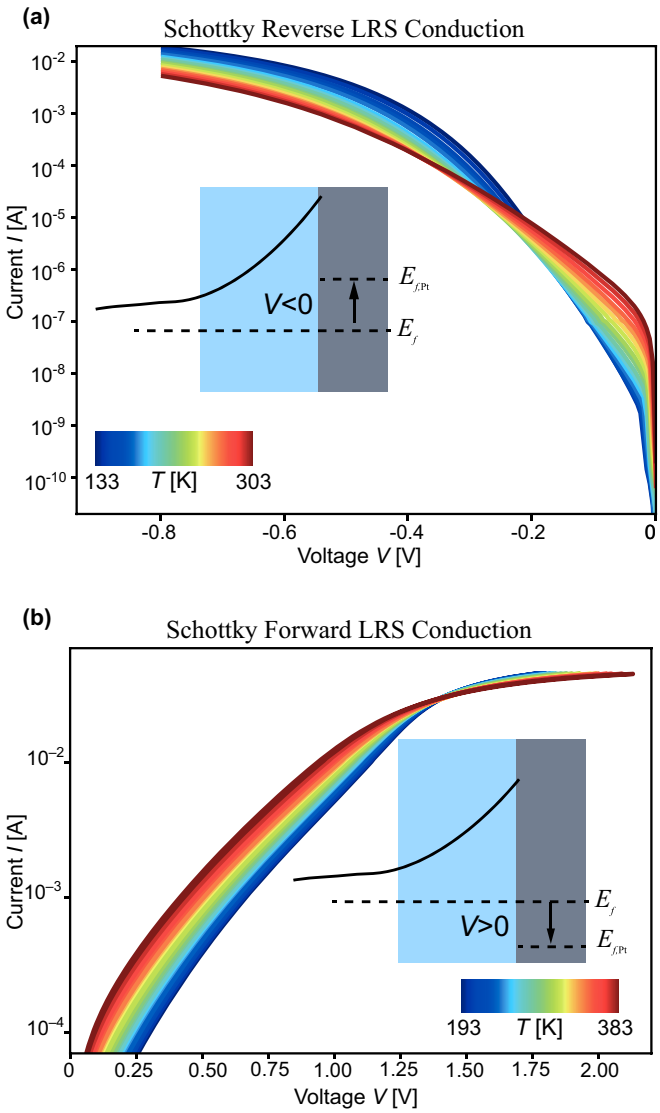

FIG. 2. (a) Experimental LRS current voltage measurement for different temperatures for the Schottky reverse direction. (b) Experimental LRS current voltage measurement for different temperatures for the Schottky forward direction. In both cases an intersection is observed.

RESET stop voltage is successively increased by $\Delta V_{\mathrm{RESET}} = -0.4$ V. All RESET sweeps are shown in Fig. 3. After each RESET sweep a READ out sweep is applied. The READ out sweeps within this study are all operated using a negative polarity meaning reverse Schottky polarity. The results of the READ out at a voltage of -0.5 V are shown in the inset of Fig. 3. It confirms that with increasing amplitude V_{RESET} a higher nonvolatile resistance state is programmed.

The electronic conduction measurements are realized using temperature-dependent READ out sweeps at each multilevel resistance state. The amplitude of the READ is kept significantly lower than the previous RESET and therefore is unable to induce a relevant ionic reconfiguration. Considering the increasing RESET force by $\Delta V_{\mathrm{RESET}}$ the measurement procedure is summarized as follows:

(1) an initial SET voltage sweep, to program the LRS,

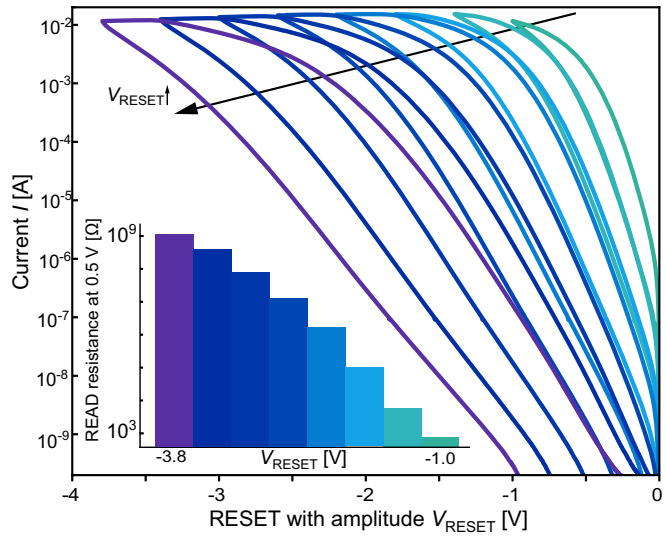

FIG. 3. Several RESET sweeps are applied in a row using different reset stop bias. The inset shows the programmed resistance states at a READ out voltage of 0.5 V.

(2) applying a RESET voltage sweep with an amplitude of V_{RESET} at a temperature of 296 K at ambient conditions,

(3) applying several READ out conduction measurements at different T under vacuum conditions,

(4) increasing the RESET stop voltage by $\Delta V_{\mathrm{RESET}}$ and turning back to step (2) with the new V_{RESET}.

The measurement sequence is sketched in Fig. 4(a) (without the single initial SET process). The READ outs are performed under vacuum conditions ($<10^{-5}$ mbar, to avoid water condensation) and for a temperature range from 133 to 303 K.

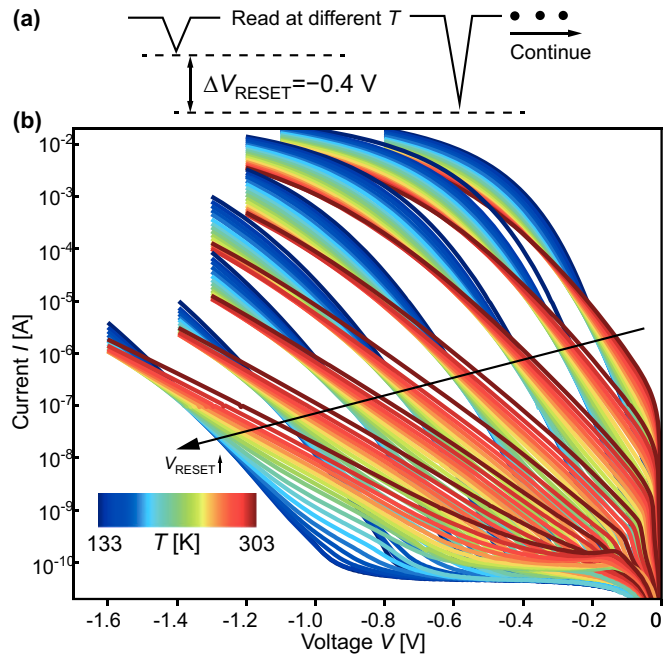

FIG. 4. (a) Sketch of the measurement sequence. (b) *I-V-T* measurements of the several resistance state programmed in Fig. 2.

The deviations of successive RESET sweeps in Fig. 3 suggest a volatile contribution, with unknown electronic or ionic origin, possibly connected to the nonstatic operation of the RESET sweeps. However, the volatile effects have a small contribution to the current response in the READ sweeps. We focus our investigation on the nonvolatile effect probed in the low-voltage READ sweeps, where the volatile contributions only have a negligible impact, justifying our discussion based on the approximation of the frozen-in ionic configuration.

All multilevel READ out *I-V* curves of the measurement procedure are given in a single plot in Fig. 4(b) for all temperatures under study. For each of the multilevel states, the measured *I-V* curves have an intersection based on their temperature dependence. In the low voltage regime, a smaller current is measured for a lower temperature. In the higher voltage regime a higher current is measured for lower temperatures. At the intermediate voltage range, the *I-V-T* curves cross each other. This voltage (-range) is named the intersection voltage V_{I}. For higher resistance states (higher $|V_{\mathrm{RESET}}|$) the intersection voltage $|V_I|$ is forced towards higher voltages. Therefore, a stronger RESET process shifts the transition point between the two temperature dependencies.

Based on the spectroscopic work of Baeumer *et al.*, it is clarified that the increasing high resistance state is a result of a decreasing oxygen vacancy concentration [23,24]. This reduction of oxygen vacancies stems from an oxygen exchange with the active electrode in this system. Unfortunately, it is not straightforward to predict the intersection and its shift based on the reduction of the oxygen vacancy concentration. To understand the physical connection between the electrical measurements and the ionic reconfiguration a simulation model has been implemented.

III. SIMULATION MODEL

Previously, the conduction of specific VCM cells was successfully described using the single band transport theory and the Wigner-Kramer-Brillouin wave-function approximation for the tunneling probability at the active electrode (in the LRS) [44,45]. Therefore, a one-dimensional simulation model based on this method is applied as well and might be further applied to other polar materials. The simulation model is restricted to the filamentary region of the $SrTiO_{3-x}$ stack and its electrode interfaces. It is considered that the current transport outside of the filament area is negligible. In the filament simulation model, the position $x = 0$ is defined as position of the ohmic electrode interface Nb:$SrTiO_3$/$SrTiO_{3-x}$. The coupled differential equation system of the simulation model is solved self-consistently including the Nb:$SrTiO_3$ region with a length of L_{Nb} and the active $SrTiO_{3-x}$ layer with a length of L_{ox}. In the simulation model, the Poisson equation

$$\nabla \cdot (\varepsilon_0 \varepsilon_r \nabla \phi) = e(n - [V_{\mathrm{O}}^{\bullet}] - 2[V_{\mathrm{O}}^{\bullet\bullet}] - [\mathrm{Nb}^{\bullet}]) \tag{1}$$

is solved to calculate the electrostatic potential ϕ. The space-charge density in the semiconductor is calculated by the concentration of the negatively charged electrons *n,* the concentration of the single positively charged oxygen vacancies $[V_{\mathrm{O}}^{\bullet}]$, doubly charged oxygen vacancies $[V_{\mathrm{O}}^{\bullet\bullet}]$, and the concentration of single positively charged Nb dopants $[\mathrm{Nb}^{\bullet}]$. The oxygen vacancies are treated as twofold donors [22]. In Eq. (1), e describes the elementary charge, ε_0 is the vacuum permittivity, and ε_r is the relative permittivity of the oxide. The Poisson equation is coupled to the charge conservation law

$$\nabla \cdot \boldsymbol{j}_{\mathrm{n}} + e\frac{\partial n}{\partial t} = G, \tag{2}$$

with the electron current density j_n, the time t, and an additional charge generation rate G, which describes the injection of tunneling electrons from and into the Pt Schottky contact. The current density is modelled by the gradient in the electrochemical potential, namely the quasi-Fermi-level E_{fn} described by

$$\boldsymbol{j}_n = \mu n \nabla E_{fn}. \tag{3}$$

Equation (3) is completed by the proportionality factors, these are the electron density n and the electron mobility μ. The boundary condition for the Poisson equation at the Nb:$SrTiO_3$ electrode is set to the ground potential

$$\Phi(x = -L_{\mathrm{Nb}}) = 0\ \mathrm{V}. \tag{4}$$

At the Pt contact, the potential is calculated from the Schottky barrier height and the externally applied voltage V:

$$\phi(x = L_{Ox}) = \phi_{\mathrm{SBH}} + \Delta\phi_{\mathrm{SBH}} + V. \tag{5}$$

In the Schottky boundary condition in Eq. (5), Φ_{SBH} is the nominal Schottky barrier height approximated from the difference in the work function of the metal and the electron affinity of the $SrTiO_3$ insulator. Additionally, the image charge based Schottky barrier lowering effect is considered by the term $\Delta\Phi_{\mathrm{SBH}}$ and defined by

$$\Delta\phi_{\mathrm{SBH}} = -\sqrt{\frac{e|\nabla\phi|}{4\pi\varepsilon_0\varepsilon_{\mathrm{r,opt}}}}. \tag{6}$$

In the Schottky barrier lowering term, the high-frequency dielectric $\varepsilon_{\mathrm{r,opt}}$ constant of $SrTiO_3$ is used. For the charge conservation law in Eqs. (2) and (3), a Dirichlet boundary condition $E_{fn} = 0$ eV is applied at the Nb:$SrTiO_3$ electrode contact. At the Schottky contact, a Neumann boundary condition is used for the charge conservation law. According to thermionic emission theory the current density over the Schottky barrier is given as

$$\boldsymbol{j}(x = L_{\mathrm{Ox}}) = \frac{A^* T}{k_{\mathrm{B}}} \int_{E_c(L_{\mathrm{ox}})}^{\infty} N_{\mathrm{top}}(L)\, dE \tag{7}$$

with the supply function of the Schottky contact

$$N_{\mathrm{top}} = k_{\mathrm{B}} T \ln\left(\frac{1 + \exp\left(-\frac{E_{\mathrm{c}} - E_{fn}}{k_{\mathrm{B}}T}\right)}{1 + \exp\left(-\frac{E_{\mathrm{c}} - E_{f\mathrm{Pt}}}{k_{\mathrm{B}}T}\right)}\right). \tag{8}$$

In Eqs. (7) and (8), E describes the energy, and $E_{f,\mathrm{Pt}}$ is the quasi-Fermi level in the Pt electrode. The energy zero level is set to the Fermi energy at zero bias. To calculate the concentration of the charge carriers, the Fermi-Dirac statistics are used. For the electron density using the single band approximation, this leads to

$$n = \frac{2N_{\mathrm{c}}}{\pi^{1/2}(k_{\mathrm{B}}T)^{3/2}} \int_0^{\infty} \frac{\sqrt{E}}{1 + \exp\left(\frac{E}{k_{\mathrm{B}}T} + \frac{E_{\mathrm{c}} - E_{fn}}{k_{\mathrm{B}}T}\right)} dE \tag{9}$$

with the effective density of states N_c. The oxygen vacancies are treated as twofold donors with the ionization energies of E_{D1} and E_{D2}. The concentration of singly charged oxygen vacancies is given by

$$[V_O^{\bullet}] = \frac{\frac{1}{2}N_{VO}\exp\left(\frac{E_c-E_{fn}}{k_BT} - \frac{E_{D1}}{k_BT}\right)}{1+\frac{1}{2}\exp\left(\frac{E_c-E_{fn}}{k_BT} - \frac{E_{D1}}{k_BT}\right)+\exp\left(2\frac{E_c-E_{fn}}{k_BT} - \frac{E_{D1}+E_{D2}}{k_BT}\right)}, \tag{10}$$

and the concentration of doubly charged oxygen vacancies

$$[V_O^{\bullet\bullet}] = \frac{N_{VO}\exp\left(2\frac{E_c-E_{fn}}{k_BT} - \frac{E_{D1}+E_{D2}}{k_BT}\right)}{1+\frac{1}{2}\exp\left(\frac{E_c-E_{fn}}{k_BT} - \frac{E_{D1}}{k_BT}\right)+\exp\left(2\frac{E_c-E_{fn}}{k_BT} - \frac{E_{D1}+E_{D2}}{k_BT}\right)}. \tag{11}$$

For the concentration of $[Nb^{\bullet}]$ it is assumed that all donors are activated and the concentration is fixed to the total Nb doping concentration. The tunneling transport across the Schottky barrier is described using the Wigner-Kramer-Brillouin approximation and implemented as in Ref. [42]. Therefore, the transmission rate T through the Schottky barrier is calculated by

$$T = \exp\left(-\frac{2}{\hbar}\int_{x_1}^{L_{Ox}}\sqrt{2m_t}\sqrt{E_c(x)-E_c(x_1)}dx\right) \tag{12}$$

with the tunneling mass m_t, the classical turning point x_1, and the Planck constant $\hbar$. The integration of additional charge carriers injected by a tunneling through the Schottky contact is integrated into the equation system by the generation rate G using the Tsu-Esaki formalism. The generation rate G is defined by

$$G = \nabla \cdot \boldsymbol{j}_{\text{tunnel}} = \frac{A^*}{k_B^2}TN_{\text{top}}\nabla E_c. \tag{13}$$

To complete the simulation model, the missing description of the electron mobility in the (Nb:)$SrTiO_{3-x}$ is required. A fundamental description regarding the scattering in polar systems has been developed by Low and Pines [46]. Their theory has been successfully applied to $SrTiO_3$ [46,47]. The mobility μ expression based on the phonon scattering in the polar crystal is given by

$$\mu_i = \frac{\hbar}{2\alpha}\frac{e}{\hbar\omega_i}\frac{e}{m_P}\left(\frac{m^*}{m_P}\right)^2 F(\alpha)\{\exp[\hbar\omega_i/(k_BT)]-1\}, \tag{14}$$

with the electron-phonon coupling constant α, the effective electron mass m^*, the polaron mass m_P, the energy of the i-th phonon mode $\hbar\omega_i$ and a slowly varying coupling function $F(\alpha)$. In the case of $SrTiO_3$, two relevant phonon modes are involved in the scattering process $i = 1, 2$) [47]. The total mobility is a result of the reciprocal addition of both μ_i. All simulation model parameters are adjusted to literature values except the electron tunneling mass m_t, where no suitable reference could be found; it is therefore fixed to the free-electron mass and its influence is considered to be small. All values are listed in Table I.

TABLE I. Simulation model input parameters.

L_{Ox}	10 nm
L_{Nb}	1 µm
$[Nb^{\bullet}]$	1.67×10^{26} m^{-3}
ε_r	100
$\varepsilon_{r,opt}$	5.7
N_C	6.9×10^{25} m^{-3}
ϕ_{SBH}	adjusted to 1.6 eV Schottky barrier height at zero electric field.
E_{D1}, E_{D2}	0.15 eV, 0.1 eV
m_t	tunneling mass is approximated by the free-electron mass m_e (9.1×10^{-31} kg)
m^*	$1.8m_e$, cf. [48]
m_P	$2.79m_e$, cf. [48]
α	3.3, cf. Ref. [48].
$F(\alpha)$	1.2 extracted from Ref. [46].
$\hbar\omega_1$, $\hbar\omega_2$,	99 meV, 58 meV

IV. RESULTS AND DISCUSSION

The experimental LRS conduction measurements in Fig. 2 show intersections in the *I-V-T* curve for both voltage polarities. The intersection at a negative polarity is found at lower voltage than the intersection at positive polarity in the sense of absolute values. To test whether the simulation model in Sec. III predicts this behavior correctly, a high oxygen vacancy concentration of 1.75×10^{27} m^{-3} is used in the model to represent the measured LRS. The simulated current response is plotted in Figs. 5(a) and 5(b) for the Schottky reverse ($V < 0$) and the Schottky forward ($V > 0$) direction, respectively. In both cases the *j-V-T* correlation shows an intersection. Like the experiment, the intersection occurs at higher absolute voltages for the forward direction compared to the reverse direction. Hence, the simulation predicts the experimental trends correctly, and the values are in the expected range of uncertainty as we will conclude at the end of this section. Therefore, the simulation can be used to understand the current transport in detail. Due to the phonon scattering described by Eq. (14), the mobility is reduced at higher temperatures. Hence, the electron mobility determines the temperature dependence of the current at voltages higher than $|V_i|$ ($>V_{i,LRS,forward}$ and $<V_{i,LRS,reversed}$). The mobility in the oxide is independent of the polarity of the applied voltage. Hence, the asymmetry in the intersection voltage in the forward and reverse direction must be an interface effect related to the active electrode. Therefore, the Schottky contact band bending is sketched for the forward and reverse direction in Figs. 5(c)–5(f). The Schottky contact sketched at small voltages in Fig. 5(d) shows that there are two physical processes stopping the electron flow at the barrier. The first process is to pass through the Schottky barrier, which is given by the quantum-mechanical tunneling probability. The second process is to gain the required thermal excitation to reach the energetic tunnel level. Before electrons can tunnel through the barrier, they must be thermally excited from the Fermi level. The second limiting process stems from the thermodynamics of electrons, which are given by the Fermi-Dirac statistic. Importantly, both processes do not equally limit the electron flow and one of them could be the dominating one. In the

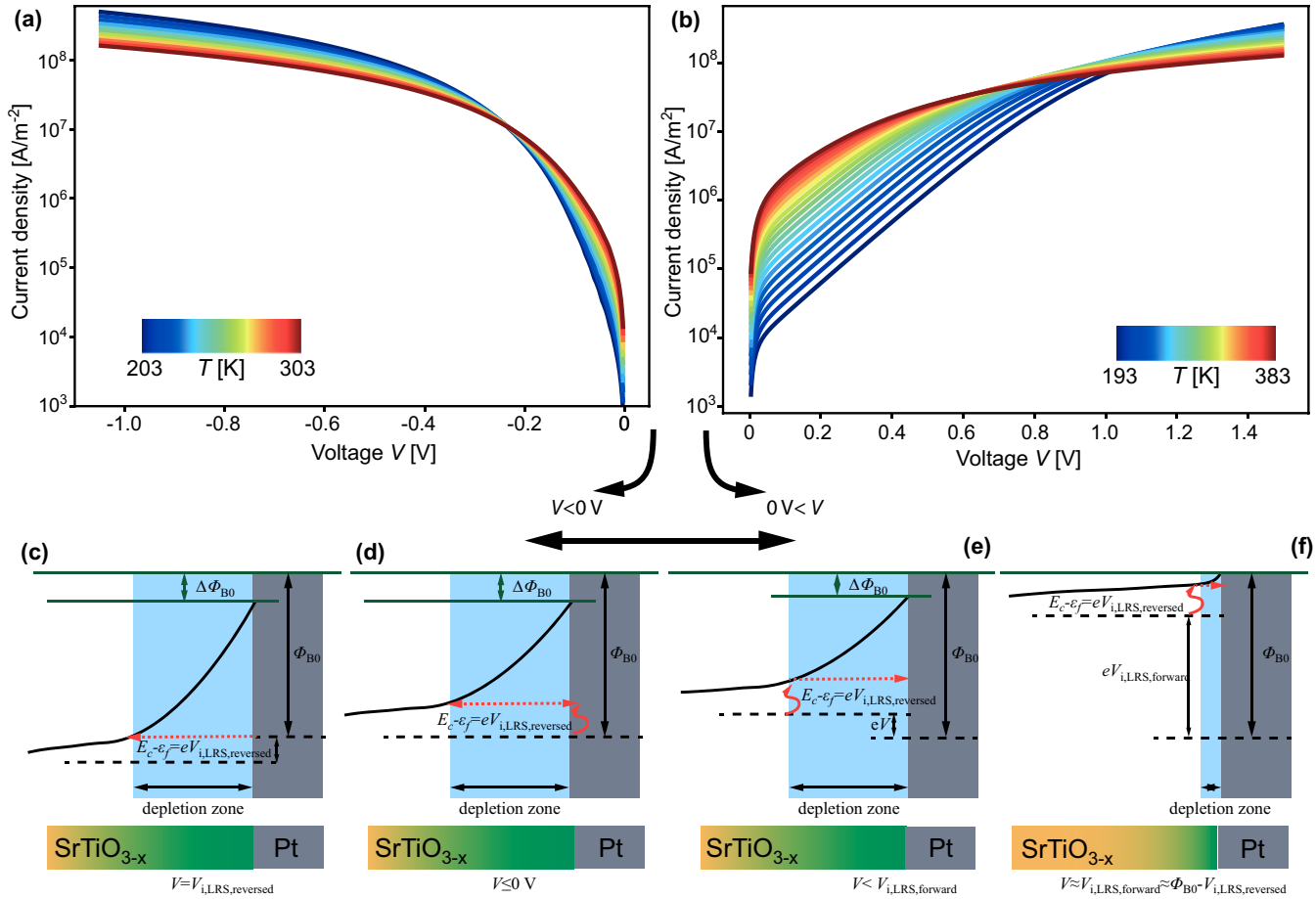

FIG. 5. (a) Schottky reverse simulated j-V characteristic for the LRS using single band transport theory. The color code represents different temperatures. (b) Schottky forward simulated j-V characteristic for the LRS at different temperatures. (c)–(f) Schottky barrier sketch at different applied voltages. The curved red line describes the thermal activation barrier. The red dashed line indicates the tunneling path. The black line describes the conduction band. The green lines stand for the undisturbed Schottky barrier ϕ_{B0} height and the image charged lowered Schottky barrier of $\phi_{B0} - \Delta\phi$.

LRS, a high concentration of oxygen vacancies is present leading to a high tunneling probability due to the shorter and lower tunneling barrier. Therefore, the thermal excitation has the major impact on the electron transport across the interface. Under this perspective the two polarities in the LRS are analyzed.

Focusing on the reverse Schottky direction in Figs. 5(c) and 5(d) the Fermi level in the metal is shifted upwards and the energetic distance to the tunneling level is lowered. This reduces the effective thermal barrier for the electrons. At the intersection voltage the metal Fermi level exceeds the tunneling level. Here the process of limited electron flow through the Schottky barrier vanishes and no thermal excitation is required. Thus, the electron flow through the Schottky barrier is only inhibited by the tunneling probability, which is comparably high in the LRS. Due to the high tunneling probability, the electron flow is not limited anymore by the interface; instead the finite mobility of electrons conducting through the oxide layer controls the electronic current.

In the Schottky forward direction, the metal Fermi level is pushed in the opposite direction towards lower energies. In this case, the electrons need to be excited from the $SrTiO_{3-x}$ quasi-Fermi level to reach the tunneling energy as shown in Figs. 5(e) and 5(f). Here, the thermal excitation process is preserved upon increasing the voltage, as indicated by the curved lines in the sketches. In contrast to the preserved thermal barrier, the upshift of the conduction band reduces the tunneling distance and barrier height. This results in a higher tunneling probability. Hence, the electron tunneling becomes more likely and the amount of electrons crossing the barrier increases. At a certain point the tunneling probability is high enough that the electron flow is limited by the transport through the bulk material instead of tunneling through the barrier, identically to the reverse Schottky direction. Hence, in both polarities the intersection is the consequence of a transition from an interface controlled to bulk/phonon controlled electron flow. The important difference in both polarities is that in the reverse direction the thermal excitation barrier is reduced and in the forward direction the tunneling barrier is reduced with increasing voltage. As the latter shows a smaller current increase with voltage, a higher voltage is required to induce the change to a bulk mobility-limited transport.

Next, we tested whether the simulation model can explain the experimentally observed multilevel switching and the shift in the intersection voltage shown in Fig. 4. To implement different resistance states in the simulation model the

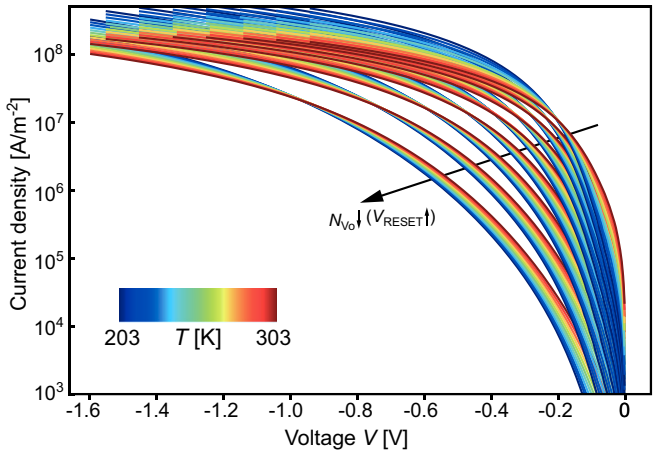

FIG. 6. Simulation of several multilevel states of the *j-V-T* behavior of several multilevel resistance states.

concentration of oxygen vacancies is modified in accordance with previous publications [23–25]. In our previous work, a comparable system shows a concentration change of oxygen vacancies of a factor of 3 for the change from LRS to HRS in the order of 10^{26} m^{-3} [23]. Hence in accordance to previous findings, the total concentration of oxygen vacancies N_{Vo} is varied in similar (but slightly higher) range from 0.75×10^{27} m^{-3} to 1.75×10^{27} m^{-3} to represent several measured multilevel resistance states. The calculated *I-V-T* curves are shown in Fig. 6. Comparing the experimental (Fig. 4) and the simulated *I-V-T* curves, a qualitatively similar behavior is observed upon reducing the oxygen vacancy concentration. All resistance states of the simulated current-voltage branches show an intersection for the different temperatures. Furthermore, the shift of the intersection voltage towards higher voltage magnitudes is also predicted correctly. Higher resistance states induced by a lower oxygen vacancy concentration have a smaller conduction and the exponential part of the *I-V* curve remains for a wider voltage range. After the intersection all multilevel states approach each other.

As a main conclusion, different oxygen vacancy concentrations in the simulation model generate several multilevel resistance states. However, the physical origin of the resistance modification and the change of the *I-V* characteristic remains unsolved, based on the previous analysis. To approach this issue the induced change in the electronic structure is identified in all resistance states. The zero voltage band diagram is analyzed for all resistance states and plotted in Fig. 7. The main influence of the reduced oxygen vacancy concentration is found directly at the active electrode interface. The inset of Fig. 7 shows that with decreasing oxygen vacancy concentration the depletion zone increases as expected from classical Schottky theory (less doping leads to a wider depletion zone; cf. Ref. [49]). In addition, the Schottky barrier height increases due to the reduced Schottky barrier lowering effect [cf. Eq. (6)]. Independent of the current transport mechanism across the Schottky barrier, a wider and higher barrier must reduce the electrical current across the interface. Therefore, the induced resistance change is an interface effect at the modified Schottky depletion zone, as sketched in Fig. 7(b). In contrast, the flat bands in the $SrTiO_{3-x}$ and the Nb:$SrTiO_3$

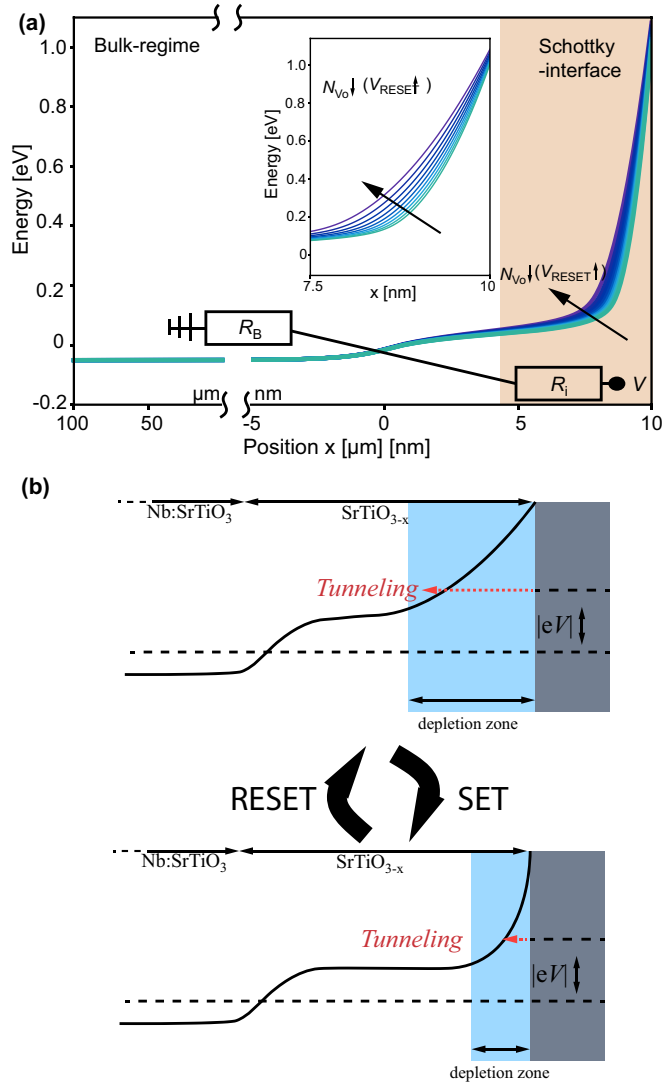

FIG. 7. (a) Zero voltage band diagram simulations for all resistance states in Fig. 4. (b) Sketch of the effect on the band diagram during a resistive switching cycle.

electrode found away from the depletion zone are unaffected by the oxygen vacancy concentration variation. Thus, the flat bands can be treated as nearly constant during the SET and RESET.

This allows us to divide the current transport into an interface contribution and a bulk transport. For a simplified picture a two resistor equivalent circuit model is established as sketched in Fig. 7(a). The first resistor is the bulk resistor R_B, which describes the band resistance through the flat bands (mainly Nb:$SrTiO_3$). As the flat bands are unaffected by the resistive switching, the resistor R_B is constant. Furthermore, the most part of the resistance R_B comes from the band conduction resistance in the Nb:$SrTiO_3$ doped electrode, which further solidifies the conclusion of a constant R_B. Therefore the modification of R_B by the change of the oxygen vacancy content is neglectable compared to the Nb:$SrTiO_3$ contribution to the bulk resistance. The physical properties defining the band resistance are given by the electron mobility, which is dominated by the phonon scattering as described in Eq. (14).

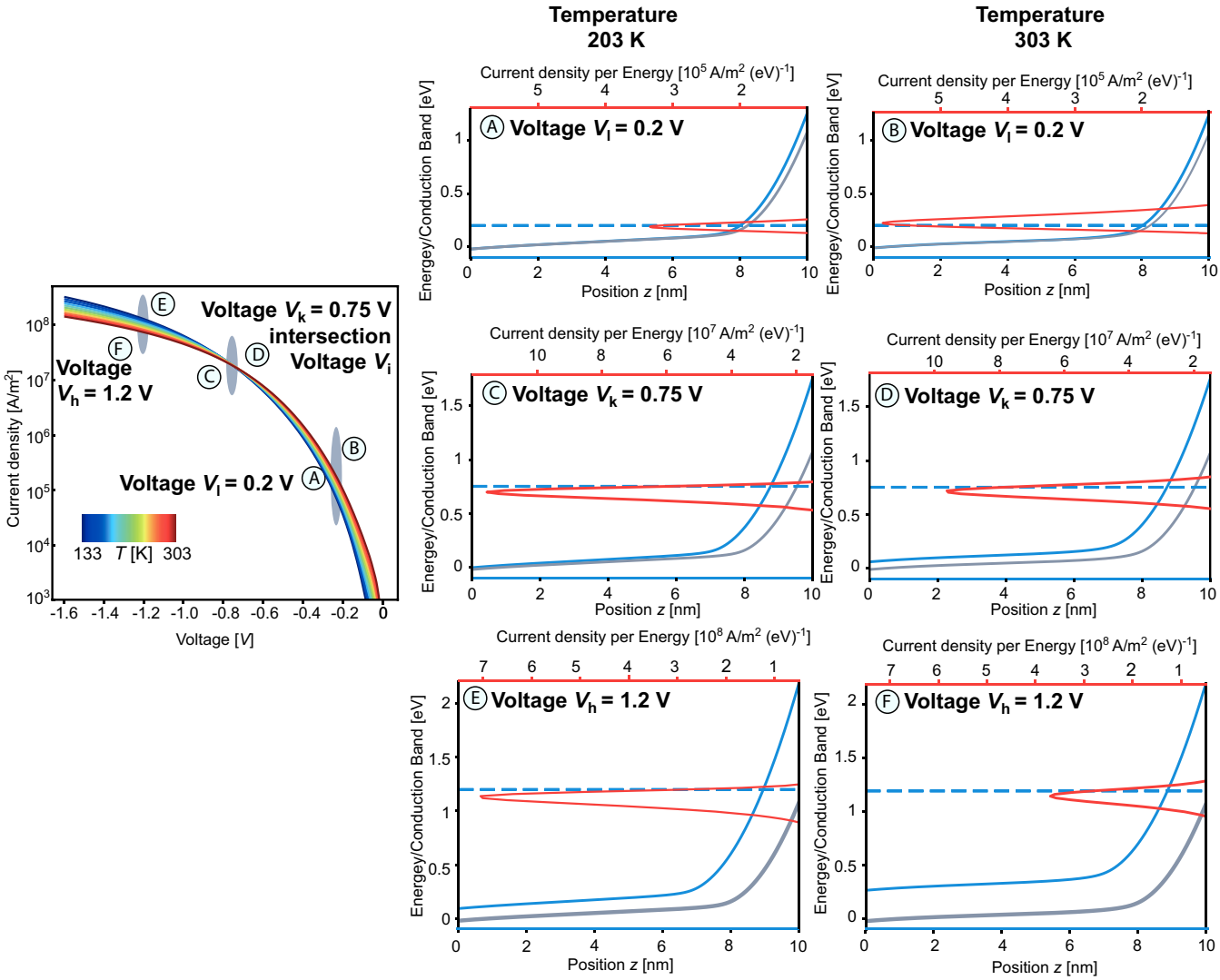

FIG. 8. Analysis of the nonzero voltage band diagram (blue) and the spectral current for an example intermediate resistance state with an intersection voltage range around 0.75 V. The grey band diagram is the zero voltage case for comparison. The oxygen vacancy concentration of this simulation has been 8.75×10^{26} m^{-3}. The positions A–F in the j-V curve correspond to the band diagram, spectral current, and temperature on the right sight of the figure.

The extension of the depletion region is small compared to the Nb:$SrTiO_3$ electrode and can therefore be neglected. The same is valid for changes of the $SrTiO_3$ layer size, when keeping it significantly below the Nb:$SrTiO_3$ size. The second resistor R_I contains the interface resistance contribution due to the Schottky barrier. As the Schottky barrier changes during SET and RESET (cf. band diagrams in Fig. 5), it is a straightforward conclusion that the interface resistor is responsible for the resistive switching effect.

To understand the change in the conduction and the change in the I-V characteristics, the previous zero voltage discussion is too superficial to approach the physics behind interface resistance change (R_I). Therefore, a more specific analysis is required, to explain the intersection and the shift of V_I to higher voltages. To detect the conduction mechanism(s) in all resistance states, we define the spectral current

$$\widehat{j}(E) = \frac{d}{dE} j. \tag{15}$$

The spectral current represents an energetic resolution of the current density in the simulation. Thus, the current at each energy level could be resolved from the simulation. Using the spectral current, it can thus be identified how much current is transmitted through the Schottky barrier into the $SrTiO_{3-x}$ conduction band at each energy.

In the following, we discuss one intermediate resistance state with a concentration of 8.75×10^{26} m^{-3} and an intersection voltage range located at near to $V_I = 0.75$ eV as an example. The isolated j-V curve is shown in Fig. 8. Here, three ranges are defined: The low voltage range (V_l), the intersection voltage range ($V_k = V_I$), and the high voltage range (V_h). In Fig. 8, the different voltage ranges are analyzed at two different temperatures ($T_1 = 203$ K, $T_2 = 303$ K). For the three voltage ranges and two temperatures, the conduction-band edge (blue) in the $SrTiO_{3-x}$ filament is compared to the zero voltage case (grey). Furthermore, the spectral current is plotted in red for each voltage range in Figs. 8A–F. All spectral currents form a peak with a maximum near the Fermi

level in the metal electrode. The interpretation of the peak is that most current passes the Schottky electrode at the peak energy level. Hence, the highest current contribution results from electron tunneling from the metal Fermi level into the $SrTiO_{3-x}$ conduction band.

The shape of the upper and lower side of the peak is determined by two different limiting mechanisms for energies above and below the Fermi edge $E_{f,\mathrm{Pt}}$. The limitation for energies lower than the metal Fermi level ($<E_{f,\mathrm{Pt}}$) stems from the reduced tunneling probability. The tunneling probability reduces with lower electron energies because of a longer tunneling distance and a higher tunneling barrier through the Schottky barrier. Hence, the reduced tunneling probability defines the lower energy side of the peak. For energies higher than the Fermi level—the upper spectral current peak side—the tunneling probability increases ($>E_{f,\mathrm{Pt}}$). Here, the current transport is limited by the thermal excitation probability, which only allows a minority of electrons to benefit from the higher tunneling probability. Hence, the upper part of the peak is formed by thermal excitation of electrons and more specifically by the Boltzmann tail of the Fermi distribution. For lower energies ($<E_{f,\mathrm{Pt}}$), the Fermi distribution is nearly constant with a value of 1 and does not play any role (tunneling limited current peak side).

Hence, the interface resistance consists of the summation of two tunneling processes. At the lower energies the electrons tunnel directly, without thermal excitation. Here, the current is limited by the broader and higher tunnel barrier. At the higher energies the amount of electrons passing the barrier is restricted to the thermal excitation rate of electrons.

For the case of an increasing temperature the peak form reshapes, especially at the upper thermal side ($>E_{f,\mathrm{Pt}}$). At higher temperatures, more electrons are thermally activated and the Fermi distribution is less steep. Hence, the spectral current peak is broader for energies above the metal Fermi level. This becomes clear by comparing the simulations at $T = 203$ K and $T = 303$ K in Fig. 8. The broader peak leads to a higher current flow.

From this consideration, the mechanism behind the interface resistance R_I is physically understood. This mechanism characterizes the voltage and temperature dependence of the interface resistance. R_I has an exponential voltage dependence as the external voltage shortens the tunneling distance and lowers the tunneling barrier. This leads to an exponentially decreasing resistance R_I with external voltage. Increasing temperatures lead to a higher tunneling contribution of thermally excited charge carriers. Hence, the resistance R_I decreases exponentially with increasing temperature. The bulk resistance R_B is voltage independent and determined by the phonon-scattering mechanism. Therefore, R_B increases with rising temperatures, which is the opposite temperature dependence of R_I. This inverse temperature dependence causes the intersection observed in all resistance states. In the low voltage range ($<|V_\mathrm{I}|$), the interface resistance dominates the total current and its temperature dependence. In the high voltage range ($>|V_\mathrm{I}|$), the bulk resistor R_B dominates and the current shows the opposite temperature dependence. The transition range from one to the other resistance defines the intersection in the *I-V-T* branches. Thus, the two competing mechanisms could be summarized as follows: The first thermally activated tunneling (R_I) stems from the Schottky interface. The second is the bulk resistance (R_B), which is dominated by the phonon interaction described in Eq. (14).

Using the two-resistor model, the intersection for all resistance states could be explained in a straightforward manner. The resistive switching is based on a modification of the tunneling properties of R_I. Hence, programming sequentially higher resistance states, as in the experimental section, increases R_I successively. In contrast, R_B remains constant during the resistive switching processes. Thus, the ratio between R_I and R_B changes. The intersection in the *I-V-T* branches is a feature of the transition between the dominating conduction mechanisms. For the increasing R_I during the RESET, the interface resistance dominates for a wider voltage range. Obviously, also the temperature dependence of R_I dominates over this broader voltage range. This mechanism shifts the transition of the dominating conduction mechanism to higher voltages. As the intersection is a consequence of the transition between the two limiting conduction mechanisms, the intersection follows the trend and occurs at higher voltages.

The two resistor model simplifies the phenomenon that the transition does not occur at one single specific voltage, but rather spreads out over a voltage range. The intersection of two *I-V* curves at different temperatures arise when the temperature dependence of the two conduction processes are canceling each other out. Thus, there is no net resistance change by going from the first to the second temperature. The temperature and voltage dependence of R_I and R_B is of different nature and strength, thus the compensation of the two mechanisms depends on the temperature. Hence, the intersection voltage depends on the chosen pair of temperatures T_1 and T_2, which results in spread out transition voltage range. Modifying the resistance states, the properties of R_I change, which also changes the transition voltage position.

Even though our model can reproduce the experimental data, two main shortcomings should be kept in mind. These effects prevent the qualitative agreement in simulation and experiment. The length of the Nb:$SrTiO_3$ electrode has been fixed to a value of 100 μm due to numerical limitations, which is shorter than in the experiment (a factor <10). This of course changes the ratio between R_B and R_I and thereby influences the absolute value of the intersection voltage. The second more critical issue is the modification of the oxygen vacancy concentration. Here, a zero-order approximation is applied by changing the total concentration homogeneously. The oxygen exchange with the electrode, however, is a rather complex mechanism. Therefore, it is not guaranteed that the oxygen vacancy concentration in the filament changes homogeneously across the whole layer thickness. An inhomogeneous modification of the oxygen vacancy concentration would influence the interface resistance and therefore could also lead to a smaller shift of the intersection voltage. Another shortcoming is the missing geometry information of the filament, which limits the power of finding a qualitative agreement between the simulation and experiment. A fitting of the numerical *I-V* curves to the experimental data would require adjusting other simulation parameters away from the literature values. Therefore, the simulations are restricted to match the qualitative trends. This avoids the overstressing of simulation parameter and losing the validity of the

simulations. Those limitations, however, do not influence the observed trends and its conclusions. Thus to cover the full complexity in the simulation a three-dimensional simulation model is required using arbitrary oxygen vacancy profiles of different concentration strength for each multilevel measured. At the current stage this is not possible with the presented model and requires further simplifications and experimental investigations.

In the VCM device the important measure is the oxygen vacancy concentration, which modifies the conduction by widening and shortening the tunneling barrier. This induces the SET or RESET and thereby the position of the intersection in the *I-V-T* curves. However, other parameters such as, for instance, the Schottky barrier height and dielectric constant would also lead to a different tunneling barrier. Thus, when changing those parameters the intersections observed here are found at different voltage positions, as the tunneling process dominates over a shorter or longer voltage range. The results, which we used here to find the electronic transport properties, are not restricted to a special Schottky barrier system or a special oxide. They are rather inherent properties of all kinds of Schottky barriers. As a result they could be transferred to other materials and the intersection may occur at other interfaces. The results may be most important for wide-band-gap material combined with high work-function metals. The electron-phonon coupling in $SrTiO_3$ is comparably strong, which makes the identification of two conduction mechanisms easy. Other systems may not have a strong enough electron-phonon interaction, which means that the intersection may not occur. In those cases, the bulk transport may not be dominated by a band transport as in amorphous materials or the transport may take place by the Poole-Frenkel conduction mechanism. Also further bulk limiting conduction mechanisms may occur, such as polaron hopping or a high doping concentration, causing a scattering at their defects. In all these cases, the transport in the bulk differs and the transition from the interface limited transport to the bulk transport would have a different shape. In those cases, no intersection would occur but there could still be a transition between two conduction mechanisms, visible by a change in the *I-V* slope.

The advantage of VCM cells is the opportunity to adjust the doping concentration intrinsically, without any other influences such as varying fabrication processes. In the field of VCM cells, the presented results are assumed to be highly relevant for systems with a strong nonlinearity in the *I-V* characteristics [50–56].

V. SUMMARY

This study presents a comprehensive understanding of the current transport through VCM cells based on the $SrTiO_3$/Pt interface, which is from the authors' point of view very likely to be generalizable to many VCM systems with an exponential *I-V* dependence. The conduction of the Nb:$SrTiO_3$/$SrTiO_3$/Pt VCM system was measured for different temperatures at both voltage polarities. Thereby the active electrode Pt-Schottky contact has a special status in the current transport. Starting with the LRS, an intersection in the *I-V-T* curves occurs, based on a change of the temperature dependence. This intersection is found for both voltage polarities, but the absolute values of the intersection voltage differ from each other. For the Schottky forward conduction, the intersection is observed at clearly higher voltages. The experiment is extended by conduction measurements at different multilevel states, which are programmed by interrupting the RESET process at different RESET stop voltages. Afterwards the *I-V-T* dependence is measured for a voltage range which is insufficient to change the resistance state. The outcome of the experiment is that all resistance states show the same intersection. However, a trend in the intersection voltage shows that it shifts to larger negative voltages with increasing resistance states. Thus, a unique behavior is observed in all resistance states, which is used to find a comprehensive physical understanding for the dominating current transport in all resistance states.

To explain the experiments, a one-dimensional simulation model is established. The electron transport is implemented by the single band transport theory combined with the Poisson equation and the charge conservation law. The tunneling into the conduction band is considered within the WKB approximation. The simulations confirm the current-voltage identity for both voltage polarities and reveal the underlying processes responsible for the intersection. In both polarities the intersection arises from a transition from an interface to a bulk controlled conduction mechanism. In the interface controlled range the Schottky barrier is overcome by a thermally assisted tunneling process. The bulk transport is limited by electron-phonon scattering. The asymmetry of the voltage intersection is based on a thermal barrier at the Schottky-type interface, which is reduced at reverse Schottky polarity and constant in the forward Schottky polarity.

Programming different multilevel states into the simulation model leads to the same shift in the intersection as has been found in the experiment. As this intersection is an event connected to changing the predominant conduction mechanism, there is a shift in the voltage ranges in which each conduction mechanism dominates. This shift in the dominating conduction mechanism range is caused by the increasing tunneling distance at the Schottky barrier. Hence, the Schottky barrier limits the transport across a larger voltage range. The extended tunneling barrier comes from the reduced amount of oxygen vacancies at the interface. This leads to the conclusion that the state variable namely the concentration of oxygen vacancies is mapped to the electronic conduction.

Within our discussion we could reduce the problem to an equivalent circuit of two resistors, which leads to a higher level of abstraction. Finding an analytical approximation for the conduction mechanism would allow us to develop a more detailed compact model of VCM resistive switching devices.

ACKNOWLEDGMENTS

This study was supported by the Deutsche Forschungs Gesellschaft (DFG) within the SFB917. C.B. received funding from the European Union's Horizon 2020 research and innovation program under Marie Sklodowska-Curie Grant Agreement No. 796142. It was partially funded by the project Advanced Computing Architectures (ACA) of the Helmholtz Initiative and Networking Fund.

[1] R. Waser, R. Dittmann, G. Staikov, and K. Szot, Redox-based resistive switching memories - Nanoionic mechanisms, prospects, and challenges, Adv. Mater. **21**, 2632 (2009).

[2] Y. Chen, B. Govoreanu, L. Goux, R. Degraeve, A. Fantini, G. Kar, D. Wouters, G. Groeseneken, J. Kittl, M. Jurczak, and L. Altimime, Balancing SET/RESET pulse for $>10^{10}$ endurance in HfO_2 1T1R bipolar RRAM, IEEE Trans. Electron Devices **59**, 3243 (2012).

[3] Y. Guo and J. Robertson, Material selection for oxide-based resistive random access memories, Appl. Phys. Lett. **105**, 223516 (2014).

[4] Y.-B. Kim, S. R. Lee, D. Lee, C. B. Lee, M. Chang, J. H. Hur, M.-J. Lee, G.-S. Park, C. J. Kim, U.-I. Chung, I.-K. Yoo, and K. Kim, Bi-layered RRAM with unlimited endurance and extremely uniform switching, in *Proceedings of the 2011 Symposium on VLSI Technology–Digest of Technical Papers, Honolulu, HI, USA* (IEEE, Piscataway, NJ, 2011).

[5] M.-J. Lee, C. B. Lee, D. Lee, S. R. Lee, M. Chang, J. H. Hur, Y.-B. Kim, C.-J. Kim, D. H. Seo, S. Seo, U.-I. Chung, I.-K. Yoo, and K. Kim, A fast, high-endurance and scalable non-volatile memory device made from asymmetric Ta_2O_{5-x}/TaO_{2-x} bilayer structures, Nat. Mater. **10**, 625 (2011).

[6] W. C. Chien, Y. C. Chen, F. M. Lee, Y. Y. Lin, E. K. Lai, Y. D. Yao, J. Gong, S. F. Horng, C. W. Yeh, S. C. Tsai, C. H. Lee, Y. K. Huang, C. F. Chen, H. F. Kao, Y. H. Shih, K. Y. Hsieh, and C. Y. Lu, A novel Ni/WOX/W resistive random access memory with excellent retention and low switching current, Jpn. J. Appl. Phys. **50**, 04DD11 (2011).

[7] M. Qi, C. Guo, and M. Zeng, Oxygen vacancy kinetics mechanism of the negative forming-free process and multilevel resistance based on hafnium oxide RRAM, J. Nanomater. **2019**, 6724018 (2019).

[8] Z. Wei, Y. Kanzawa, K. Arita, Y. Katoh, K. Kawai, S. Muraoka, S. Mitani, S. Fujii, K. Katayama, M. Iijima, T. Mikawa, T. Ninomiya, R. Miyanaga, Y. Kawashima, K. Tsuji, A. Himeno, T. Okada, R. Azuma, K. Shimakawa, H. Sugaya *et al.*, Highly reliable TaOx ReRAM and direct evidence of redox reaction mechanism, in *Proceedings of the 2008 IEEE International Electron Devices Meeting, San Francisco, CA, USA* (IEEE, Piscataway, NJ, 2008).

[9] Z. Wei, T. Takagi, Y. Kanzawa, Y. Katoh, T. Ninomiya, K. Kawai, S. Muraoka, S. Mitani, K. Katayama, S. Fujii, R. Miyanaga, Y. Kawashima, T. Mikawa, K. Shimakawa, and K. Aono, Demonstration of high-density ReRAM ensuring 10-year retention at 85°C based on a newly developed reliability model, in *Proceedings of the 2011 International Electron Devices Meeting, Washington, DC, USA* (IEEE, Piscataway, NJ, 2011).

[10] B. J. Choi, A. C. Torrezan, K. J. Norris, F. Miao, J. P. Strachan, M.-X. Zhang, D. A. A. Ohlberg, N. P. Kobayashi, J. J. Yang, and R. S. Williams, Electrical performance and scalability of Pt dispersed SiO_2 nanometallic resistance switch, Nano Lett. **13**, 3213 (2013).

[11] V. Havel, K. Fleck, B. Rösgen, V. Rana, S. Menzel, U. Böttger, and R. Waser, Ultrafast switching in Ta_2O_5-based resistive memories, in *Proceedings of the Silicon Nanoelectronics Workshop SNW 2016, Hawaii, Honolulu* (IEEE, Piscataway, NJ, 2016), pp. 82–83.

[12] S. Menzel, M. von Witzleben, V. Havel, and U. Boettger, The ultimate switching speed limit of redox-based restive switching devices, Faraday Discuss. **213**, 197 (2019).

[13] A. C. Torrezan, J. P. Strachan, G. Medeiros-Ribeiro, and R. S. Williams, Sub-nanosecond switching of a tantalum oxide memristor, Nanotechnology **22**, 485203 (2011).

[14] B. Govoreanu, G. S. Kar, Y-Y. Chen, V. Paraschiv, S. Kubicek, A. Fantini, I. P. Radu, L. Goux, S. Clima, R. Degraeve, N. Jossart, O. Richard, T. Vandeweyer, K. Seo, P. Hendrickx, G. Pourtois, H. Bender, L. Altimime, D. J. Wouters, J. A. Kittl, and M. Jurczak, 10×10 nm^2 Hf/HfO_x crossbar resistive RAM with excellent performance, reliability and low-energy operation, in *Proceedings of the 2011 International Electron Devices Meeting, Washington, DC, USA* (IEEE, Piscataway, NJ, 2011).

[15] S. Pi, C. Li, H. Jiang, W. Xia, H. Xin, J. J. Yang, and Q. Xia, Memristor crossbar arrays with 6-nm half-pitch and 2-nm critical dimension, Nat. Nanotechnol. **14**, 35 (2019).

[16] V. V. Zhirnov, R. Meade, R. K. Cavin, and G. Sandhu, Scaling limits of resistive memories, Nanotechnology **22**, 254027 (2011).

[17] M. Witzleben, K. Fleck, C. Funck, B. Baumkötter, M. Zuric, A. Idt, T. Breuer, R. Waser, U. Böttger, and S. Menzel, Investigation of the impact of high temperatures on the switching kinetics of redox-based resistive switching cells using a highspeed nanoheater, Adv. Electron. Mater. **3**, 1700294 (2017).

[18] J. J. Yang, M. D. Pickett, X. Li, D. A. A. Ohlberg, D. R. Stewart, and R. S. Williams, Memristive switching mechanism for metal/oxide/metal nanodevices, Nat. Nanotechnol. **3**, 429 (2008).

[19] A. Hardtdegen, C. La Torre, F. Cüppers, S. Menzel, R. Waser, and S. Hoffmann-Eifert, Improved switching stability and the effect of an internal series resistor in HfO_2/TiO_x bilayer ReRAM cells, IEEE Trans. Electron. Devices **65**, 3229 (2018).

[20] V. Havel, A. Marchewka, S. Menzel, S. Hoffmann-Eifert, G. Roth, and R. Waser, Electroforming of Fe:STO samples for resistive switching made visible by electrocoloration observed by high resolution optical microscopy, MRS Online Proc. Libr. **1691**, mrss14–1691-bb03–09 (2014).

[21] A. Kindsmueller, A. Meledin, J. Mayer, R. Waser, and D. J. Wouters, On the role of the metal oxide/reactive electrode interface during the forming procedure of valence change ReRAM devices, Nanoscale **11**, 18201 (2019).

[22] C. Linderälv, A. Lindman, and P. Erhart, A unifying perspective on oxygen vacancies in wide band gap oxides, J. Phys. Chem. Lett. **9**, 222 (2018).

[23] C. Baeumer, C. Schmitz, A. Marchewka, D. N. Mueller, R. Valenta, J. Hackl, N. Raab, S. P. Rogers, M. I. Khan, S. Nemsak, M. Shim, S. Menzel, C. M. Schneider, R. Waser, and R. Dittmann, Quantifying redox-induced Schottky barrier variations in memristive devices via in operando spectromicroscopy with graphene electrodes, Nat. Commun. **7**, 12398 (2016).

[24] D. Cooper, C. Baeumer, N. Bernier, A. Marchewka, C. La Torre, R. E. Dunin-Borkowski, S. Menzel, R. Waser, and R. Dittmann, Anomalous resistance hysteresis in oxide ReRAM: Oxygen evolution and reincorporation revealed by *in situ* TEM, Adv. Mater. **29**, 1700212 (2017).

[25] H. Zhang, S. Yoo, S. Menzel, C. Funck, F. Cüppers, D. J. Wouters, C. S. Hwang, R. Waser, and S. Hoffmann-Eifert, Resistive switching modes with opposite polarity in $Pt/TiO_2/Ti/Pt$ nano-sized ReRAM devices, ACS Appl. Mater. Interfaces **10**, 29766 (2018).

[26] Z. Wang, H. Wu, G. W. Burr, C. S. Hwang, K. L. Wang, Q. Xia, and J. J. Yang, Resistive switching materials for information processing, Nat. Rev. Mater. **5**, 173 (2020).

[27] S. Slesazeck and T. Mikolajick, Nanoscale resistive switching memory devices: A review, Nanotechnology **30**, 352003 (2019).

[28] D. Ielmini and R. Waser, *Resistive Switching—From Fundamentals of Nanoionic Redox Processes to Memristive Device Applications* (Wiley-VCH, Weinheim, Germany, 2016).

[29] M. Aono, T. Nakayama, T. Sakamoto, H. Hihara, K. Takeuchi, I. Valov, R. Waser, K. Terabe, T. Hasegawa, T. Tsuruoka, S. Watanabe, T. Tsuchiya, and R. Aguilera, *Atomic Switch: From Invention to Practical Use and Future Prospects* (Springer International Publishing, Cham, Switzerland, 2020).

[30] S. Yu, B. Gao, Z. Fang, H. Yu, J. F. Kang, and H.-S. P. Wong, A low energy oxide-based electronic synaptic device for neuromorphic visual systems with tolerance to device variation, Adv. Mater. **25**, 1774 (2013).

[31] K. Seo, I. Kim, S. Jung, M. Jo, S. Park, J. Park, J. Shin, K. P. Biju, J. Kong, K. Lee, B. Lee, and H. Hwang, Analog memory and spike-timing-dependent plasticity characteristics of a nanoscale titanium oxide bilayer resistive switching device, Nanotechnology **22**, 254023 (2011).

[32] T. Wan, B. Qu, H. Du, X. Lin, Q. Lin, D. W. Wang, C. Cazorla, S. Li, S. Liu, and D. Chu, Digital to analog resistive switching transition induced by graphene buffer layer in strontium titanate based devices, J. Colloid Interface Sci. **512**, 767 (2018).

[33] T. Shi, R. Yang, and X. Guo, Coexistence of analog and digital resistive switching in $BiFeO_3$-based memristive devices, Solid State Ionics **296**, 114 (2016).

[34] B. Long, Y. Li, and R. Jha, Switching characteristics of $Ru/HfO_2/TiO_{2-x}$/Ru RRAM devices for digital and analog nonvolatile memory applications, IEEE Electron Device Lett. **33**, 706 (2012).

[35] M. Prezioso, F. Merrikh-Bayat, B. D. Hoskins, G. C. Adam, K. K. Likharev, and D. B. Strukov, Training and operation of an integrated neuromorphic network based on metal-oxide memristors, Nature (London) **521**, 61 (2015).

[36] S. Yu, B. Gao, Z. Fang, H. Yu, J. Kang, and H. Wong, Stochastic learning in oxide binary synaptic device for neuromorphic computing, Front. Neurosci. **7**, 186 (2013).

[37] M. Hu, C. E. Graves, C. Li, Y. Li, N. Ge, E. Montgomery, N. Davila, H. Jiang, R. S. Williams, J. J. Yang, Q. Xia, and J. P. Strachan, Memristor-based analog computation and neural network classification with a dot product engine, Adv. Mater. **30**, 1705914 (2018).

[38] S. H. Jo, T. Chang, I. Ebong, B. B. Bhadviya, P. Mazumder, and W. Lu, Nanoscale memristor device as synapse in neuromorphic systems, Nano Lett. **10**, 1297 (2010).

[39] C. Funck, A. Marchewka, C. Baeumer, P. C. Schmidt, P. Mueller, R. Dittmann, M. Martin, R. Waser, and S. Menzel, A theoretical and experimental view on the temperature dependence of the electronic conduction through a schottky barrier in a resistively switching $SrTiO_3$-based memory cell, Adv. Electron. Mater. **4**, 1800062 (2018).

[40] C. Baeumer, C. Funck, A. Locatelli, T. O. Mente F. Genuzio, T. Heisig, F. Hensling, N. Raab, C. M. Schneider, S. Menzel, R. Waser, and R. Dittmann, In-gap states and band-like transport in memristive devices, Nano Lett. **19**, 54 (2019).

[41] N. Raab, C. Bäumer, and R. Dittmann, Impact of the cation-stoichiometry on the resistive switching and data retention of$SrTiO_3$thin films, AIP Adv. **5**, 047150 (2015).

[42] A. Marchewka, B. Roesgen, K. Skaja, H. Du, C. L. Jia, J. Mayer, V. Rana, R. Waser, and S. Menzel, Nanoionic resistive switching memories: On the physical nature of the dynamic reset process, Adv. Electron. Mater. **2**, 1500233 (2016).

[43] T. Heisig, C. Baeumer, U. N. Gries, M. P. Mueller, C. La Torre, M. Luebben, N. Raab, H. Du, S. Menzel, D. N. Mueller, C.-L. Jia, J. Mayer, R. Waser, I. Valov, R. A. De Souza, and R. Dittmann, Oxygen exchange processes between oxide memristive devices and water molecules, Adv. Mater. **30**, 1800957 (2018).

[44] G. Wentzel, Eine Verallgemeinerung der Quantenbedingungen für die Zwecke der Wellenmechanik, Z. Phys. **38**, 518 (1926).

[45] H. A. Kramers, Wellenmechanik und halbzahlige Quantisierung, Z. Phys. **39**, 828 (1926).

[46] F. Low and D. Pines, Mobility of slow electrons in polar crystals, Phys. Rev. **98**, 414 (1955).

[47] A. Verma, A. P. Kajdos, T. A. Cain, S. Stemmer, and D. Jena, Intrinsic Mobility Limiting Mechanisms in Lanthanum-Doped Strontium Titanate, Phys. Rev. Lett. **112**, 216601 (2014).

[48] H. P. R. Frederikse and W. Hosler, Hall mobility in $SrTiO_3$, Phys. Rev. **161**, 822 (1967).

[49] S. M. Sze and K. K. Ng, *Physics of Semiconductor Devices* (Wiley, Hoboken, New Jersey, 2007).

[50] G. Sassine, S. La Barbera, N. Najjari, M. Minvielle, C. Dubourdieu, and F. Alibart, Interfacial versus filamentary resistive switching in TiO_2 and HfO_2 devices, J. Vacuum Sci. Technol. B **34**, 12202 (2016).

[51] Y. Ding, X. Xu, A. Bhalla, X. Yang, J. Chen, and C. Chen, Switchable diode effect in $BaZrO_3$ thin films, RSC Adv. **6**, 60074 (2016).

[52] M. Zhao, Y. Zhu, Y. Zhang, T. Zhang, D. Qiu, G. Lai, C. Hu, Q. Wang, F. Zhang, and M. Li, Resistive switching and related magnetization switching in Pt/BiFeO3/Nb:$SrTiO_3$ heterostructures, RSC Adv. **7**, 23287 (2017).

[53] H. Li, Y. Xia, B. Xu, H. Guo, J. Yin, and Z. Liu, Memristive behaviors of $LiNbO_3$ ferroelectric diodes, Appl. Phys. Lett. **97**, 12902 (2010).

[54] C. Oh, S. Heo, H. M. Jang, and J. Son, Correlated memory resistor in epitaxial $NdNiO_3$ heterostructures with asymmetrical proton concentration, Appl. Phys. Lett. **108**, 122106 (2016).

[55] J. Guyonnet, I. Gaponenko, S. Gariglio, and P. Paruch, Conduction at domain walls in insulating $Pb(Zr_{0.2}Ti_{0.8})O_3$ thin films, Adv. Mater. **23**, 5377 (2011).

[56] C. C. Lin, B. C. Tu, C. C. Lin, C. H. Lin, and T. Y. Tseng, Resistive switching mechanisms of V-doped $SrZrO_3$ memory films, IEEE Electron Device Lett. **27**, 725 (2006).